Article

Nanoparticles as an antidote for poisoned gold single-atom catalysts in sustainable propylene epoxidation

Qianhong Wang[1,3], Keng Sang[1,3], Changwei Liu[1,3], Zhihua Zhang[1], Wenyao Chen[1]✉, Te Ji[2], Lina Li[2], Cheng Lian[1], Gang Qian[1], Jing Zhang[1], Xinggui Zhou[1]✉, Weikang Yuan[1] & Xuezhi Duan[1]✉

The development of sustainable and anti-poisoning single-atom catalysts (SACs) is essential for advancing their research from laboratory to industry. Here, we present a proof-of-concept study on the poisoning of Au SACs, and the antidote of Au nanoparticles (NPs), with trace addition shown to reinforce and sustain propylene epoxidation. Multiple characterizations, kinetics investigations, and multiscale simulations reveal that Au SACs display remarkable epoxidation activity at a low propylene coverage, but become poisoned at higher coverages. Interestingly, Au NPs can synergistically cooperate with Au SACs by providing distinct active sites required for H_2/O_2 and C_3H_6 activations, as well as hydroperoxyl radical to restore poisoned SACs. The difference in reaction order between C_3H_6 and H_2 (n_{C3H6}-n_{H2}) is identified as the descriptor for establishing the volcano curves, which can be fine-tuned by the intimacy and composition of SACs and NPs to achieve a rate-matching scenario for the formation, transfer, and consumption of hydroperoxyl. Consequently, only trace addition of Au NPs antidote (0.3% ratio of SACs) stimulates significant improvements in propylene oxide formation rate, selectivity, and H_2 efficiency compared to SACs alone, offering a 56-fold, 3-fold, and 22-fold increase, respectively, whose performances can be maintained for 150 h.

Single-atom catalysts (SACs) capture significant interest in catalysis by virtue of their maximum atom utilization, tunable electronic properties, and special size quantum effects, which afford superior catalytic performances across a wide range of catalytic reactions[1–4]. Despite various approaches developed for the large-scale synthesis of SACs with uniform and well-defined atomic structures, SACs are not guaranteed to provide a more efficient and sustainable catalytic conversion than their nanoparticle counterparts[5–7]. Apart from their poor thermal stability under severe conditions, SACs encounter notable obstacles including variable reactant adsorption capabilities and limited active sites[8]. On the one hand, SACs may exhibit either too strong or too weak adsorption capability for certain reactants or intermediates[9–11]. On the other hand, they fail to provide the cooperativity between different types of active sites required for complex reactions that involve the activation, adsorption and migration of reactants and intermediates[12–14]. These two difficulties pose significant challenges for SACs in reactions involving multiple reactants or the formation of intermediates that require stabilization before undergoing subsequent reactions[15,16]. Hence, it is of fundamental importance to explore and develop new strategies to overcome these two difficulties for extending the SACs from laboratorial synthesis to industrial application.

[1]State Key Laboratory of Chemical Engineering, East China University of Science and Technology, 130 Meilong Road, Shanghai 200237, China. [2]Shanghai Synchrotron Radiation Facility, Shanghai Advanced Research Institute, Shanghai 201210, China. [3]These authors contributed equally: Qianhong Wang, Keng Sang, Changwei Liu. ✉e-mail: wenyao.chen@ecust.edu.cn; xgzhou@ecust.edu.cn; xzduan@ecust.edu.cn

The direct epoxidation of propylene with H_2/O_2 to value-added propylene oxide (PO) using bifunctional Au-Ti catalysts ($C_3H_6 + H_2 + O_2 \rightarrow C_3H_6O + H_2O$) is considered a dream reaction for PO production[17,18]. It is widely accepted that hydrogen peroxide or hydroperoxyl intermediate generated by H_2 and O_2 on Au sites would transfer and react with C_3H_6 on adjacent Ti sites to generate PO, and neither Au nor Ti alone would give any significant PO activity[19,20]. As such, the manipulation of Ti coordination environment and Au particle size are the two main tools to improve catalytic performances[21–24]. However, there is currently an intense debate on the role of Au particle size in this reaction, as different sizes ranging from 2–5 nm[25], 1–2 nm[26], 1.4 nm[27], ~1 nm[28], <1 nm[29], or 0.7 nm[30] have been suggested as Au active site. Rationally, this debate can be attributed to the use of different Ti supports (TiO_2, TS-1, Ti-SBA-15, TiO_2/SiO_2, and Ti-SiO$_2$) and related preparation details (Si/Ti ratio, calcination, and pore structure), yielding different Au-Ti synergies and catalytic results. Moreover, as far as we are concerned, tiny Au clusters, even Au single atoms (SAs), have rarely been tested for this reaction, despite Au_3 being predicted as an active site based on DFT calculations[31]. Hence, it is highly desirable to eliminate the Ti effects to obtain a thorough understanding of Au size effects from nanoscale to subnanoscale and even single atom, which will help form a complete picture to refine the design principle of Au catalyst.

In this study, we report the fabrication of a series of Au catalysts anchored on Ti-free silicalite-1 (S-1) support to obtain the isolated Au SAs (Au_1), Au NPs (Au_n), as well as their coexistences ($Au_{1\&n}$) for propylene epoxidation. Both the PO formation rate and selectivity, as well as H_2 efficiency exhibit volcano curves as a function of Au size, with $Au_{1\&n}$ exhibiting the best catalytic performance. It is demonstrated that Au SACs display an attractive epoxidation activity at a low propylene surface coverage, but become poisoned by its strong adsorption at higher coverage. However, Au NPs can provide hydroperoxyl radical for reacting with C_3H_6 on Au SAs, thus lowering C_3H_6 coverage to restore Au SAs. Simultaneously, Au NPs can cooperate with Au SAs to provide different types of active sites required for the activation of H_2/O_2 and C_3H_6, respectively. Hence, Au_n can serve as the antidote for Au_1 catalyst to overcome the above two representative problems associated with SACs. Furthermore, the difference in reaction order between C_3H_6 to H_2 ($n_{C_3H_6}$-n_{H_2}) is identified as catalytic descriptor to establish the volcano curves, which can be fine-tuned by the intimacy and composition of Au SACs and Au NPs to achieve the reactant coverage-matching. As a result, only trace addition of Au NPs (0.3% ratio of Au SACs) can stimulate a simultaneous increase in PO formation rate from 10.4 to 583.6 $mol_{PO}\cdot mol_{Au}^{-1}\cdot h^{-1}$, PO selectivity from 25.1%–75.6%, and H_2 efficiency from 1.4% to 30.5%, whose catalytic performances can be maintained for 150 h.

Results

Catalyst preparation and characterization

As discussed above, the prerequisite to make a fair comparison of Au size effects remains to alleviate the disturbance of Ti species. However, this contradicts the formation of PO over Au-Ti bifunctional catalysts, while the monometallic Au in the absence of Ti primarily yields acrolein[32,33]. This discrepancy was first explored by first-principles theoretical calculations with periodic density functional theory (DFT) on a representative Au(111) surface. We calculated a variety of possible adsorption sites, and identified the reaction pathways starting from propylene and hydroperoxyl based on previous studies[34,35]. As a result, two pathways for PO formation were considered in Supplementary Fig. 1, involving hydroperoxametallacycle (HO-OMC) formation or hydroperoxyl dissociation, both leading to the same precursor of a five-member ring oxametallacycle (OMMC) and a subsequent four-member one (OMC). The transformation of OMMC into PO was identified as the rate-determining step (RDS) with an energy barrier of 1.11 eV. For acrolein formation (Supplementary Fig. 2), the RDS involves

the attack of allyl intermediates by oxygen from hydroperoxyl dissociation with the energy barrier of 1.10 eV. The similar energy barrier for PO and acrolein generation indicates that PO has the similar possibility as acrolein to be produced on monometallic Au, which motivates us to study Au size effects in the absence of Ti.

Accordingly, using uncalcined S-1 as support to suppress catalyst deactivation from pore blocking by carbonaceous deposits, we prepared a series of Au/S-1 catalysts by deposition-precipitation method, and the nominal and actual Au loadings were summarized in Supplementary Table 1. As characterized by HAADF-STEM in Supplementary Figs. 3–10, lowering Au loadings from 0.460 wt% to 0.026 wt% can decrease Au particle size from 3.9 to 2.1 nm (Supplementary Table 1), based on the measurement of >150 random particles. The high dispersion and small size of Au NPs were also confirmed by the XRD patterns in Supplementary Fig. 11. As shown in Fig. 1a–c, further decreasing Au loading from 0.014 wt% to 0.004 wt% significantly lowers Au NPs density and size, making it difficult to distinguish Au sites. Hence, aberration-corrected HAADF-STEM was employed to characterize the catalysts with the loading of 0.004, 0.014, and 0.026 wt%, which consist of isolated Au SAs (labeled by the red circle in Fig. 1d and Supplementary Fig. 10), a mixture of Au SAs and NPs (Fig. 1e), and Au NPs (labeled by the blue square in Fig. 1f), respectively. In this regard, the three catalysts were denoted as Au_1, $Au_{1\&n}$, and Au_n, in which the absence of Au NPs for Au_1 catalyst is consistent with its ultralow loading (0.004 wt%).

The XPS spectra in Fig. 1g exhibit a continuous increase of Au $4f$ binding energy by decreasing Au size, most likely attributed to the final state effect resulting from the size-dependent electrostatic interaction between ionized cluster and escaping photoelectron[36]. Moreover, the negative shift of Au $4f$ binding energy of these catalysts compared with bulk Au indicates electron transfer from S-1 – Au nanoparticles for these catalysts, and the resultant electron-rich Au species has been suggested to weaken oxygen adsorption to promote this reaction[37]. Correspondingly, there is a significant decrease in signal intensity, particularly for Au_1, whose signal was too weak to be detectable. Notably, although there are some isolated Au SAs in the $Au_{1\&n}$ catalyst, most of Au atoms are ensembled, and the metallic character still dominates, similar to the Au_n catalyst. Unfortunately, XAS failed to gain more insights into their electronic structures and coordination environments due to the low Au loadings. In this regard, we conducted in-situ synchrotron-based FTIR (SR-FTIR) measurements with a smaller spot size and faster acquisition capability, enabling us to obtain high-quality spectral imaging data from a synchrotron light source. A comparison of the C−H stretching vibrations of C_3H_6, represented by the band ranging from 2935 – 3015 cm^{-1} [38], was made in Fig. 1h. Au_1 only exhibits a slightly decreased adsorption of C_3H_6 compared to Au_n, despite its ultralow Au loading. However, Fig. 1i reveals a noticeable red shift of 2 cm^{-1} for the Au_n catalyst with respect to the Au_1 catalyst. This shift is most likely attributed to the higher electron density of Au NPs compared to Au SAs, agreeing well with the above Au $4f$ binding energy shift.

Catalytic performances and kinetics investigations

The catalytic performances of these catalysts for propylene epoxidation were summarized in Supplementary Table 2, and compared in Fig. 2a. Both PO formation rate and selectivity as well as H_2 efficiency exhibit volcano curves as a function of Au loading, with $Au_{1\&n}$ catalyst providing the highest catalytic performance of 80.2 $mol_{PO}\cdot mol_{Au}^{-1}\cdot h^{-1}$ than Au_1 (10.4 $mol_{PO}\cdot mol_{Au}^{-1}\cdot h^{-1}$) and Au_n (25.9 $mol_{PO}\cdot mol_{Au}^{-1}\cdot h^{-1}$) catalyst. Moreover, PO emerges as the main product for $Au_{1\&n}$ catalyst with the selectivity of 55.2%, while propanal and acrolein dominate the product distribution at the left and right side of the volcano curve, respectively. After minimizing the effects of internal and external diffusion limitations as shown in Supplementary Table 3, the activation energy for each catalyst was determined based on the corresponding
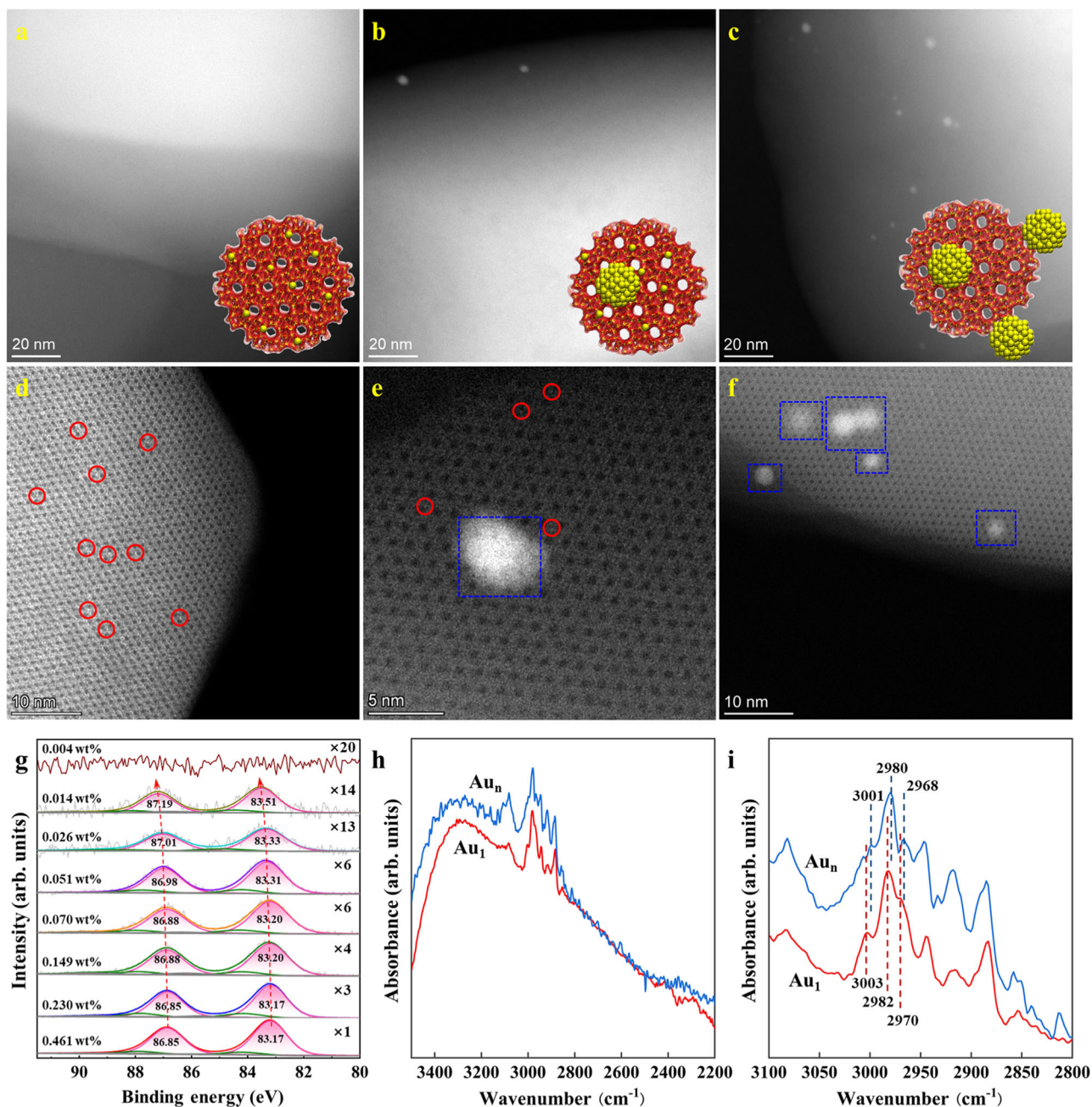
Fig. 1 | Structural characterization of Au$_1$, Au$_{1\&n}$, and Au$_n$. a–c HAADF-STEM images in low magnification of Au$_1$ (**a**), Au$_{1\&n}$ (**b**), and Au$_n$ (**c**) catalyst. **d–f** Aberration-corrected HAADF-STEM images in high magnification of Au$_1$ (**d**), Au$_{1\&n}$ (**e**), and Au$_n$ (**f**) catalyst. **g**, XPS Au 4f spectra of Au/S-1 catalysts with different loadings. **h, i** In-situ SR-FTIR spectra of C$_3$H$_6$ adsorption (**h**) and that in the range of 2800-3100 cm^{-1} (**i**) of the Au$_1$ and Au$_n$ catalyst at 40 ℃. The Au loadings for the Au$_1$, Au$_{1\&n}$, and Au$_n$ catalysts are 0.004, 0.014, and 0.026 wt%, respectively.

Arrhenius plots in Supplementary Fig. 12, and is shown in Fig. 2b, in which Au$_{1\&n}$ catalyst has the lowest activation energy (23.0 kJ·mol^{-1}) followed by Au$_n$ (28.7 kJ·mol^{-1}) and Au$_1$ (46.3 kJ·mol^{-1}). Interestingly, the activation energy further decreases with increasing Au loading, reaching a minimal of 9.4 kJ·mol^{-1} for the catalyst with the loading of 0.460 wt%. The decrease in activation energy seems in contrast to the lowest catalytic performance observed for this catalyst, suggesting that reactant adsorption, rather than activation, can be the main cause for its poor catalytic performance in Fig. 2a. Hence, in addition to studying the effects of reaction temperature in related to the activation, we have investigated the effects of reactants concentration in related to the adsorption as shown in Supplementary Figs. 13–15, and the resultant reaction orders are further compared in Fig. 2c.

Interestingly, the reaction order of either H$_2$ or C$_3$H$_6$ varies dramatically with Au loading, where that of H$_2$ continuously decreases from 0.73 to -0.40, compensated by an increase of C$_3$H$_6$ from 0.20 to 0.78. Comparatively, the reaction order for O$_2$ exhibits a slight decrease regardless of the amount of Au loaded onto the catalyst. All of these observations indicate a negligible change in O$_2$ surface coverage, but a strong competitive adsorption between H$_2$ and C$_3$H$_6$ on the catalyst surface. Specifically, the surfaces of Au$_1$ and Au$_n$ catalyst are mainly covered by C$_3$H$_6$ and H$_2$, respectively, consistent with the above in-situ SR-FTIR results. Moreover, an unexpected shift in kinetic isotope effects (KIE) from normal (Au$_1$ catalyst) to inverse ones (Au$_n$ catalyst) is observed in Fig. 2d. In general, inverse KIE are typically associated with variations in the steric environment of the active site
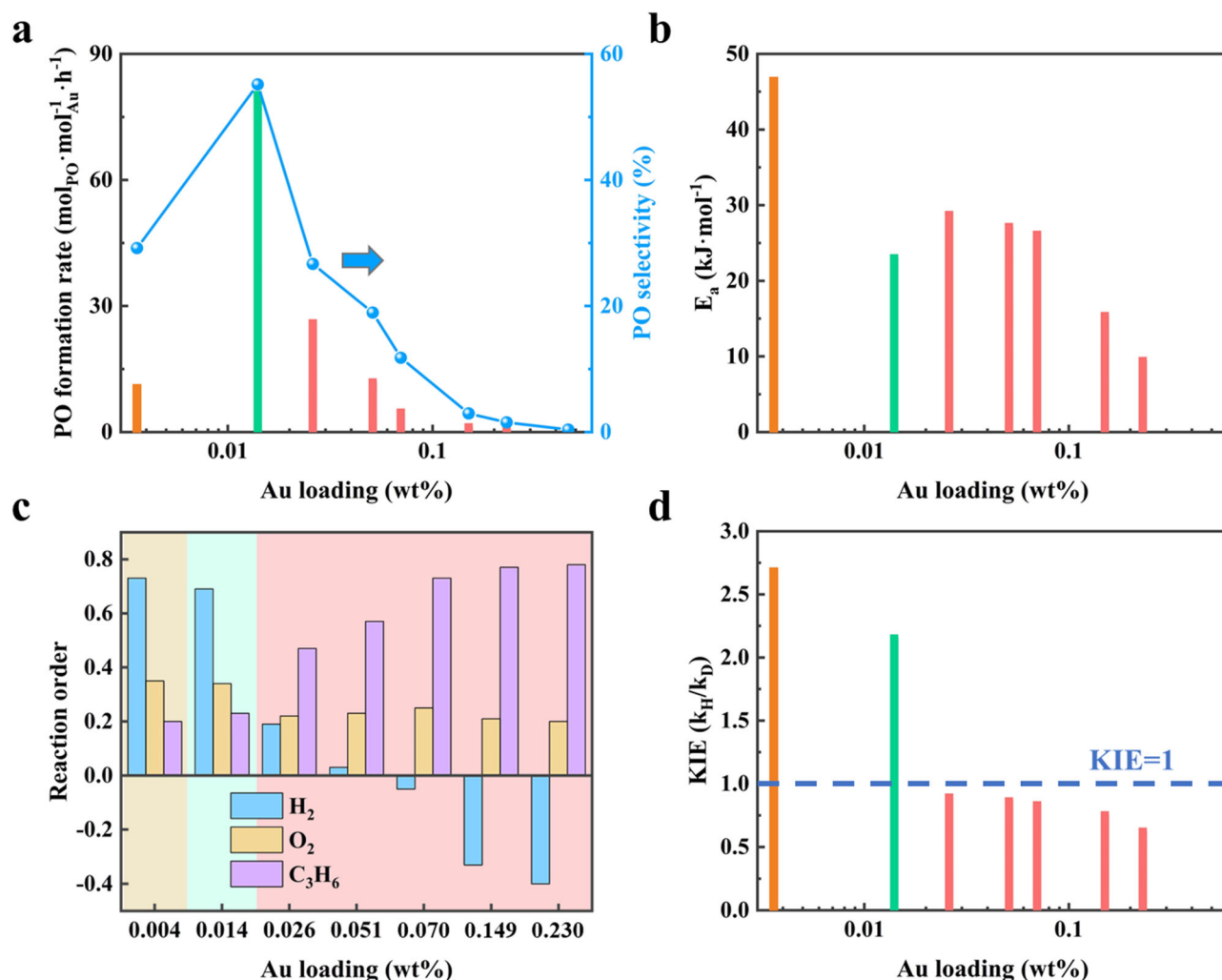
Fig. 2 | Catalytic performance and kinetic investigations. a–d PO formation rate and selectivity (**a**), activation energy (**b**), reaction order of H_2, O_2, and C_3H_6 (**c**), as well as kinetic isotope effects (**d**) of the Au/S–1 catalysts with different loadings.

due to deuteration during RDS[39–41]. In this case, since the D atom is heavier than the H atom, the stronger D-D and C-D bonds could result in shorter bond lengths compared to the H-H and C-H bonds[42]. Consequently, the shorter D-D and C-D bonds can lead to a less obstructed active site and facilitates a less hindered pathway for reactants, resulting in the observed inverse KIE for the Au_n catalyst, which aligns with its surface being covered by hydrogen. Accordingly, the Au_1 and Au_n catalysts under reaction conditions are mainly covered by C_3H_6 and H_2, respectively. This explains why the Au catalyst with the highest loading (0.460 wt%) is probably poisoned by H_2 to exhibit the most negative reaction order of -0.40 as well as the poorest activity, despite having the lowest activation energy. In contrast, the moderate reaction orders of C_3H_6 and H_2, as well as KIE, suggest a trade-off of surface coverage between C_3H_6 and H_2 for the $Au_{1\&n}$ catalyst, which affords its highest catalytic performance among these catalysts.

Mechanistic insights into the poisoning of Au SACs

To gain mechanistic insights into the significantly different epoxidation activity among the Au_1, $Au_{1\&n}$, and Au_n catalyst, we first performed DFT calculations on Au single atom, Au_{13} cluster, and Au(111) surface. Accordingly, Au single atom and Au_{13} cluster models on silicalite-1 surface were constructed via an investigation of different local structures of Au species in Supplementary Figs. 16, 17, respectively. The charge population for Au atom, obtained by integrating the projected density of state (PDOS) up to the Fermi level as shown in

Supplementary Fig. 18, is determined to be 8.82 e. This implies an almost complete transfer of one d electron from the Au atom to S-1, which is consistent with the observed binding energy shift in XPS spectra. The reaction pathways of propylene epoxidation on Au single atom, Au_{13} cluster, and Au(111) surface are exhibited in Fig. 3a, with the corresponding structural configurations displayed in Supplementary Figs. 19–21. It can be seen that all these models initiate with the reaction between O_2 and H_2 to generate hydroperoxyl radical and hydrogen adatom. Subsequently, the hydroperoxyl dissociates into the active oxygen species over Au(111), which will react with C_3H_6 to form oxametallacycle as propylene oxide precursor. The rate-determining step (RDS) is identified as the hydroperoxyl formation $(O_2^* + H_2^* \rightarrow OOH^* + H^*)$ with an energy barrier of 1.57 eV. In contrast, the active oxygen species derived from hydroperoxyl dissociation can directly react with C_3H_6 to produce PO over Au_{13} cluster without the formation of oxametallacycle, which is identified as the RDS with an energy barrier of 0.25 eV. Interestingly, the Au single atom can further simply the reaction pathway by directly catalyzing the reaction between the hydroperoxyl radical and C_3H_6 into PO with the lowest energy barrier (0.20 eV), shifting the RDS back to the hydroperoxyl formation with an energy barrier of 0.31 eV.

As shown in Fig. 3b, the smaller-sized Au species including Au single atom and Au_{13} cluster can greatly lower the energy barrier to promote PO generation. This is consistent with the higher activity of subnano-sized metal species compared to metal NPs in many
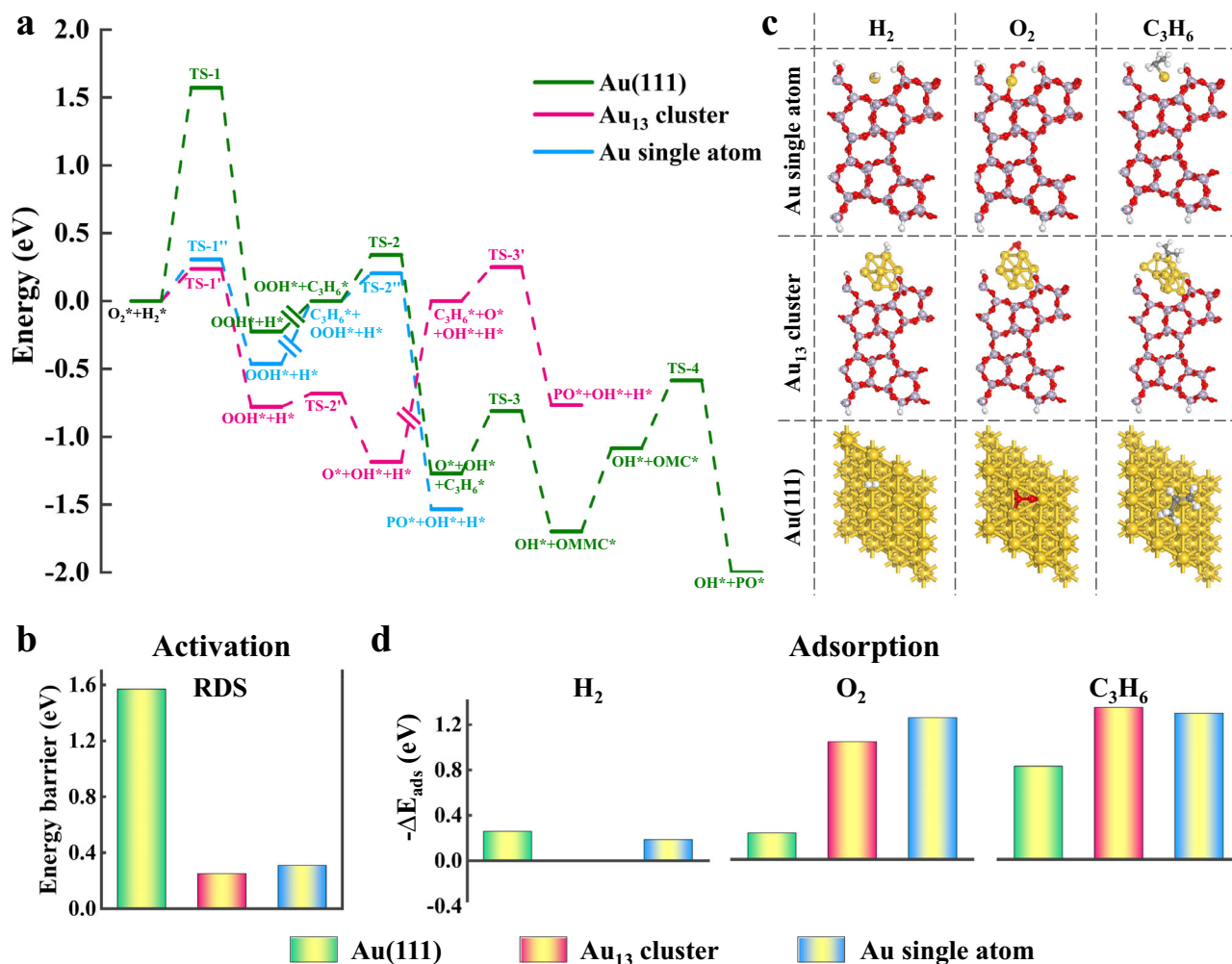
Fig. 3 | Theoretical calculation on propylene adsorption and activation.
a–d Calculated energy profile for propylene epoxidation (**a**), the corresponding energy barrier of rate-determining step (**b**), most energy-favorable adsorption configurations of O_2, H_2, and C_3H_6 (**c**), and the corresponding adsorption energies (ΔE_{ads}) (**d**) over Au single atom, Au_{13} cluster, and Au(111) surface.

reactions. However, this contradicts the poorest catalytic performance of Au_1 catalyst with the highest composition of Au SAs than $Au_{1\&n}$ and Au_n catalyst. According to the kinetics investigation described above, not only the activations of reaction species but also their adsorptions have profound effects on this reaction. In this regard, we further compared the adsorption of reactants and products over Au single atom, Au_{13} cluster, and Au(111) surface. The adsorptions of H_2, O_2, and C_3H_6 were investigated in Supplementary Figs. 22–24, and their adsorption geometries were computed for the top, bridge, and 3-fold hollow sites. Accordingly, the most energy-favorable adsorption configurations are displayed in Fig. 3c, and the corresponding adsorption energies are summarized in Fig. 3d. Obviously, H_2 binds very weakly with Au single atom, Au_{13} cluster, and Au(111) surface. In comparison, both O_2 and C_3H_6 exhibit much higher adsorption energies on Au single atom, Au_{13} cluster than them on Au(111) surface. Accordingly, Au single atom prefers to strongly interact with C_3H_6 rather than H_2, as also suggested by the low reaction order for C_3H_6 and high reaction order for H_2.

Hence, based on DFT calculations, it is suggested that Au SAs exhibit high catalytic activity for propylene epoxidation at low propylene coverage, but could be poisoned under high surface coverages. To provide a more comprehensive understanding, we conducted a combination of reactive molecular dynamics (RMD) and classical molecular dynamics (CMD) to simulate the reaction for the Au_1 catalyst

as shown in Supplementary Movie 1, and the resulting initial and final snapshots are presented in Supplementary Figs. 25, 26, respectively. As depicted in Fig. 4a, gas molecules undergo strong interactions and accumulate over the catalyst surface, with some molecules even penetrating into the silicalite-1 framework. The statistic concentration profiles shown in Fig. 4b exhibit distinct number density distributions of H_2, O_2, and C_3H_6 along the z-axis. The high-density regions of O_2 and C_3H_6 are ~2.0 Å away from Au SAs, while that of H_2 is around 5.0 Å. This implies that O_2 and C_3H_6 molecules tend to form a solvation layer over the catalyst surface, which in turn impedes the accessibility of hydrogen molecules to the catalyst surface.

The radial distribution functions (RDFs) of H_2, O_2, and C_3H_6 around Au SAs are further analyzed in Supplementary Fig. 27 to get an in-depth understanding of molecule interactions. The peak at 2.1 Å is associated with the nearest neighbor distance between Au SAs and propylene, whose intensity is much stronger than that of 2.3 Å for Au SAs and oxygen. Moreover, two additional peaks at 2.6 and 3.0 Å can be observed for C_3H_6, arising from its adsorption configuration of $\mu_1\eta^1(CH_2)$ in Supplementary Fig. 27. In contrast, hydrogen exhibits the nearest neighbor distance of 2.8 Å with the weakest intensity. These findings suggest the highest probability of finding C_3H_6 molecules around Au SAs, which is the lowest for H_2. Based on the RDFs results, we select the neighbor distance of 2.25 Å as the statistical criterion for strong chemical adsorption around Au SAs, and studied the dynamic
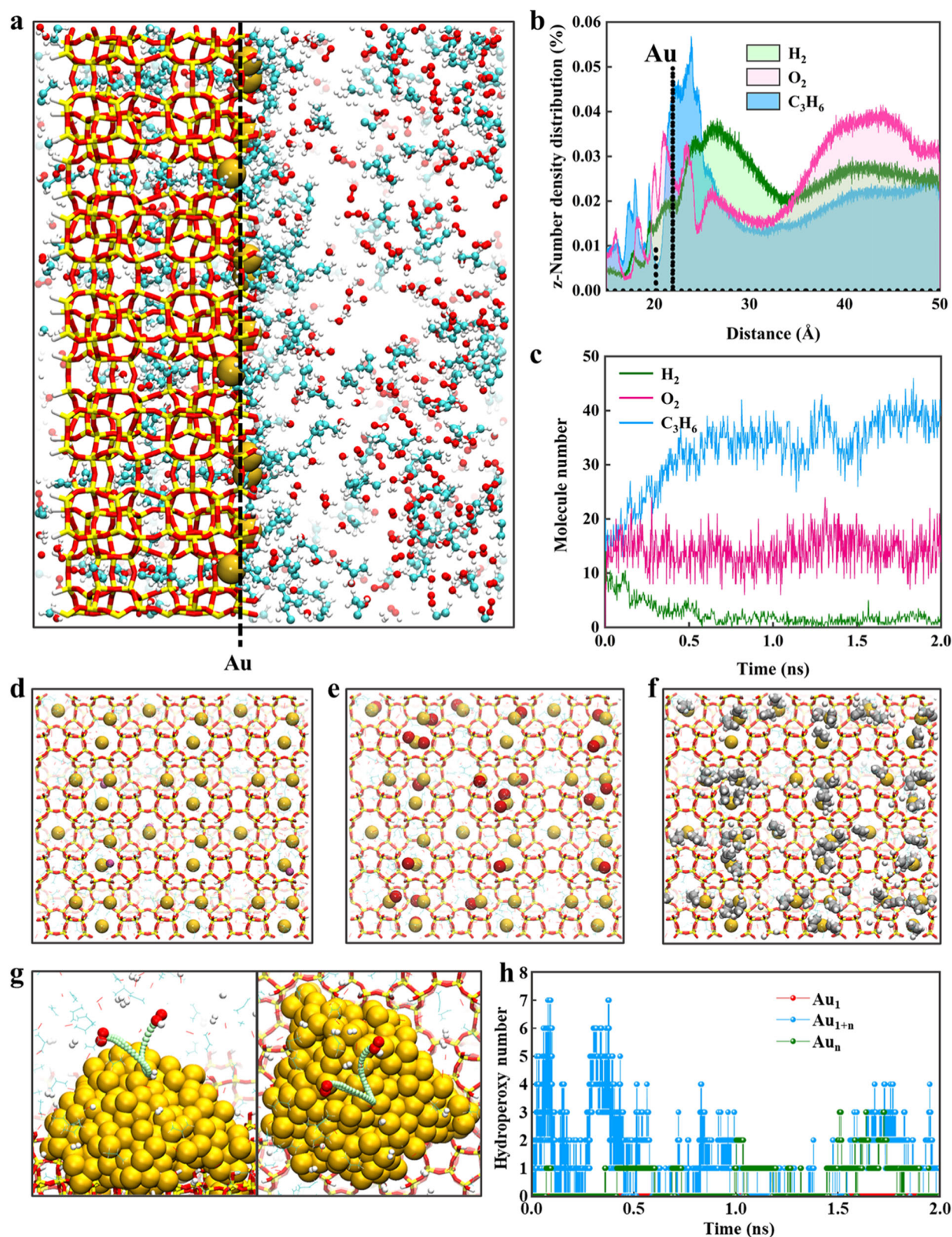
Fig. 4 | RMD simulation on the poisoning of Au SACs. a, b Representative snapshot (**a**), and the corresponding number density distributions of H_2, O_2, and C_3H_6 (**b**) over Au_1 catalyst along the z-axis. The data is based on the well-equilibrated configuration of a 2.0 ns for the RMD-CMD simulations. **c** The number of adsorbed H_2, O_2, and C_3H_6 over Au_1 catalyst as a function of RMD-CMD simulation time. **d–f** Representative snapshots of the adsorption of H_2 (**d**), O_2 (**e**), and C_3H_6 (**f**) on Au SAs at 2.0 ns for the RMD-CMD simulations. **g** The reaction path for the production of hydroperoxy intermediate from H_2 and O_2 over Au NPs. **h** The number of hydroperoxy intermediate over the Au_1, $Au_{1\&n}$, and Au_n catalyst as a function of RMD-CMD simulation time.

adsorption process of different molecules. As shown in Fig. 4c, the numbers of different gas molecules adsorbed on Au SAs were almost the same after a low-temperature relaxation. However, when the temperature rapidly rose to the target temperature of 473 K, the number of adsorbed H_2 dropped to almost zero compensated by a significant increase in C_3H_6, while that of O_2 remained almost unchanged. Consequently, as illustrated in Fig. 4d–f, Au SAs were easily occupied by numerous C_3H_6 molecules with negligible H_2 adsorption, where only a few O_2 molecules can dissociate into adsorbed oxygen atoms. All these results provide a dynamic picture of the poisoning of Au SAs by C_3H_6 adsorption.

Furthermore, we have conducted the same simulations for the $Au_{1\&n}$ and Au_n catalyst to get more information about the reaction, and the corresponding initial and final snapshots are presented in Supplementary Figs. 28–31. In comparison to the Au_1 catalyst, which was poisoned by C_3H_6 with minimal reaction occurring, the presence of Au NPs promotes the formation of hydroperoxyl radical from H_2 and O_2 as shown in Supplementary Movie 2 and Supplementary Fig. 32. Moreover, the corresponding reaction pathway is displayed in Fig. 4g, where the gaseous O_2 molecule approaches the catalyst surface, and reacts with the adsorbed H_2 molecule to generate the hydroperoxyl intermediate. The hydroperoxyl intermediate then desorbs from Au NPs to the gas phase for its further conversion, and such a process is consistent with the above DFT calculations. In this regard, a comparison of the number of the generated hydroperoxyl radical was made for the Au_1, $Au_{1\&n}$, and Au_n catalyst. As shown in Fig. 4h, the number of hydroperoxyl radical increases with the reaction temperature for the latter two catalysts, particularly for $Au_{1\&n}$, whose number can reach a maximum of 7. Upon reaching the target temperature of 473 K, its number decreases and then fluctuates, indicating a reaction balance between its formation, transfer, and consumption. Conversely, its number remains negligible for the Au_1 catalyst throughout the entire process. In this regard, Au NPs can work with Au SAs for the coverage-matching between different reactants to promote the balance between the formation, transfer, and consumption of hydroperoxyl radical.

## Volcano curves and catalytic descriptor

To this point, although DFT calculations predict that Au SAs are highly active for catalyzing propylene epoxidation, kinetic (isotope) studies, and RMD-CMD simulations have shown that they are easily poisoned by the strong adsorption of C_3H_6. As a result, Au_1 catalyst with a high composition of Au SAs exhibits lower catalytic performances than Au_n catalyst. On the other hand, Au NPs exhibit a weak binding with H_2, O_2, and C_3H_6, allowing the reaction between hydrogen and oxygen to generate the active hydroperoxyl radical. The hydroperoxyl radical can then transfer to adjacent Au SAs and react with the adsorbed C_3H_6 to produce PO. From an adsorption point of view, Au NPs can help complete the catalytic cycle by lowering C_3H_6 coverage and restoring more active sites. From an activation point of view, Au NPs can synergistically cooperate with Au SAs to provide different types of active sites required for the activation of H_2/O_2 and C_3H_6, respectively. Therefore, Au NPs can serve as an antidote for Au SAs to overcome the two widely-recognized challenges faced by single-atom catalysts. Combining the merits of both Au SAs and Au NPs, $Au_{1\&n}$ catalyst exhibits the highest catalytic performance for PO production.

It is worth to note that the above $Au_{1\&n}$ catalyst is still dominated by the metallic character of Au NPs rather than the ionized character of Au SAs (Fig. 1g). In this regard, we further tried to maximize Au atom utilization by investigating the intimacy and composition of Au SAs and Au NPs as shown in Fig. 5. At a given composition of Au_n to Au_1 ($Au_n:Au_1 = 1:3$), it can be seen in Fig. 5a that the catalyst with a dual bed manner, which provides a "millimeter-scale" distance between Au SAs and Au NPs, exhibits a higher catalytic performance than either Au_1 or Au_n alone. By further shortening the proximity between Au_1 and Au_n to a micrometer-scale distance through mortar mixing, the highest PO

formation rate of 170.1 $mol_{PO} \cdot mol_{Au}^{-1} \cdot h^{-1}$ is achieved, which is >16 times higher than that of the Au_1 catalyst. Additionally, the improved epoxidation rate is accompanied by a continuously increased H_2 efficiency in Supplementary Table 4, indicating more conversion of hydroperoxyl into PO rather than water. The results suggest that the intimacy between Au_1 and Au_n strongly affects the catalytic performance, with long spatial distances making the transfer of hydroperoxyl radical and the subsequent propylene epoxidation difficult. Such mass transfer effect in tandem process was also observed and proposed as the "intimacy criterion", which was first proposed by Weisz on investigating isomerization and hydrocracking[43]. Moreover, the corresponding kinetics study in Supplementary Fig. 33 gives the reaction order of 0.28, 0.31, and 0.35 for H_2, O_2, and C_3H_6, respectively. Obviously, the addition of Au_n into Au_1 catalyst can significantly lower the reaction order of H_2 compensated with an increase of C_3H_6 reaction order. This implies the reduced C_3H_6 surface coverage to alleviate its poisoning for more H_2 adsorption and reaction.

Tailoring the composition of Au_1 and Au_n, as a representative of the number of Au SAs and Au NPs, on the micrometer-scale intimacy can further improve the catalytic performance, as depicted by the volcano curve as shown in Fig. 5b and Supplementary Table 5. Surprisingly, the mortar mixing of a few Au_n to Au_1 catalyst in a ratio of 1:7 offers a 56-fold improvement in activity (583.6 $mol_{PO} \cdot mol_{Au}^{-1} \cdot h^{-1}$), 3-fold improvement in PO selectivity (75.6%), as well as 22-fold improvement in H_2 efficiency (30.5%) compared to Au_1 single-atom catalyst. The almost linear correlation between PO formation rate and H_2 efficiency as shown in Supplementary Fig. 34 indicates a rate-matching scenario for the formation, transfer, and consumption of hydroperoxyl radical to maximize the catalytic performances. It is worth to note that this PO formation rate even outperforms a majority of Au-Ti bifunctional catalysts in previous studies (Supplementary Table 6). Meanwhile, we have conducted the in-situ SR-FTIR measurement of C_3H_6 desorption, in which the band ranging from 2935 to 3015 cm^{-1} was compared in Fig. 5c, where the influences of C_3H_6 adsorption on S-1 support could be excluded as shown in Supplementary Fig. 35. Obviously, the substitution of Au_1 by Au_n catalyst significantly lowers the amount and strength of C_3H_6 adsorption over the mixed catalyst surface. Additionally, we have also investigated the corresponding reaction orders, and the results are illustrated in Supplementary Figs. 36–40 and summarized in Supplementary Table 7. Evidently, the reaction order of C_3H_6 increases with the substitution of Au_1 by Au_n catalyst, while the trend is completely reversed for H_2, further confirming the compromise between C_3H_6 and H_2 adsorption.

Considering all the catalysts mentioned above, the difference in reaction order between C_3H_6 and H_2, denoted as n_{C3H6}-n_{H2}, can serve as an indicator of the competition between C_3H_6 and H_2 adsorption, and correlate with the catalytic performance in Figs. 6a–c. It can be seen that both the PO formation rate and selectivity as well as H_2 efficiency exhibit volcano curves as a function of n_{C3H6}-n_{H2}, where the reaction is limited by the poisoning adsorption of C_3H_6 at the left side and H_2 at the right side. As a result, C_3H_6 mainly converts into propanal and acrolein over the catalyst surface mainly covered by C_3H_6 and H_2, respectively. In order to produce PO, the reactant surface coverages can be fine-tuned by the intimacy and composition of Au SAs and Au NPs. Hence, from the perspective of mesokinetics[14], n_{C3H6}-n_{H2} is identified as the catalytic descriptor for quantitively correlating the microscopic properties of active sites, including the intimacy and composition of Au SAs and Au NPs, with the macroscopic catalytic performance, which can predict catalytic function and screen catalysts. Accordingly, the mortar-mixing catalyst ($Au_n:Au_1 = 1:7$) is suggested to achieve the coverage-matching with moderate n_{C3H6}-n_{H2} in Fig. 6a–c, thus contributing to a rate-matching scenario with the highest catalytic performance. The stability of such catalyst was also tested as shown in Fig. 6d, whose reaction rate can be maintained for 150 h without a significant decrease. The observed high stability is
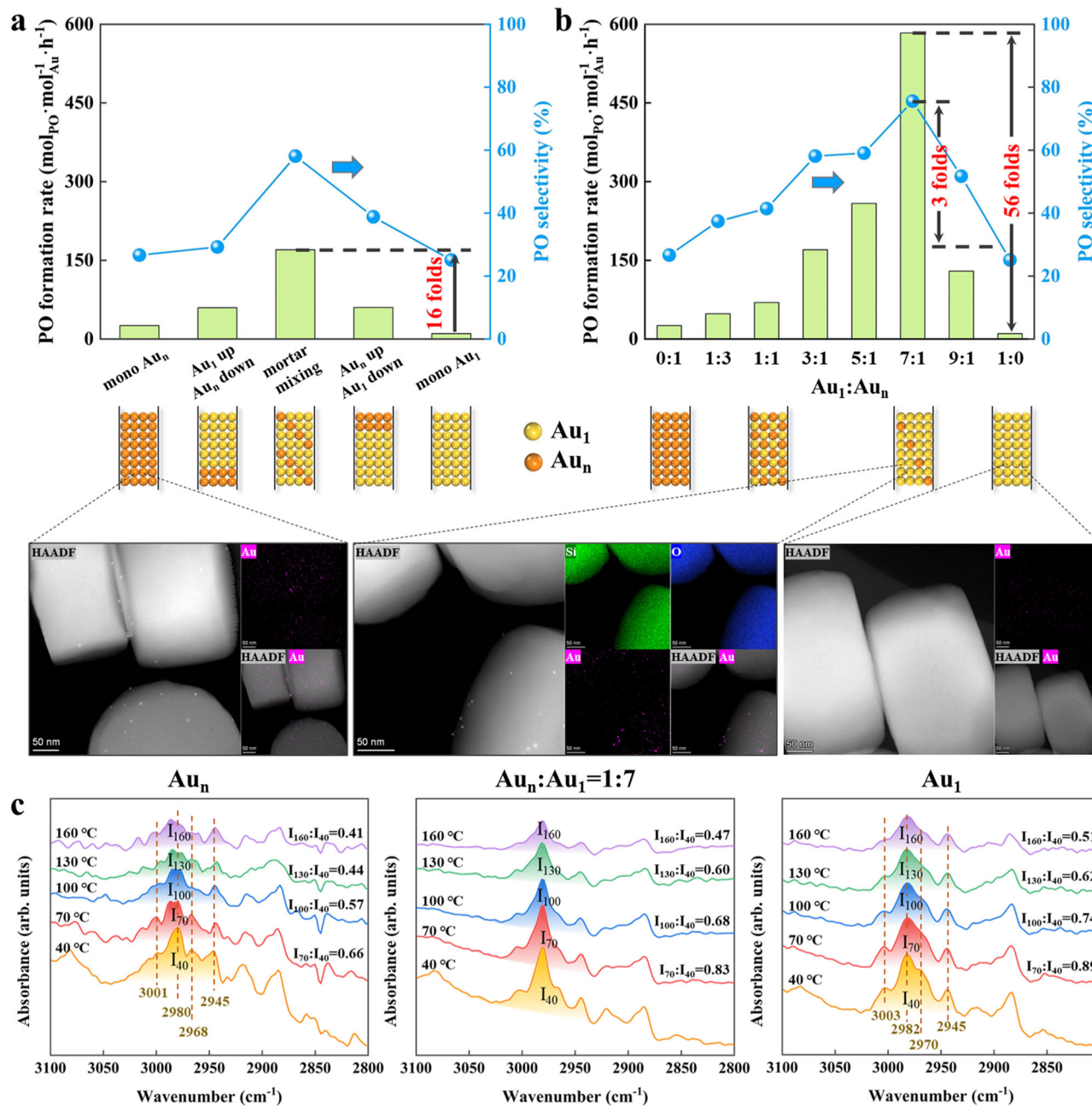
Fig. 5 | Effects of intimacy and composition of Au SAs and Au NPs. a, b PO formation rate and selectivity for mixing Au_1 and Au_n in different intimacies (**a**) and compositions (**b**). **c** In-situ SR-FTIR spectra of C_3H_6 desorption for the Au_n, mortar-mixing catalyst ($An_n:Au_1 = 1:7$), and Au_1 catalyst at elevated temperatures.

likely due to the robust interactions between Au single atoms and the S-1 support, as depicted in Supplementary Fig. 41, effectively hindering site agglomeration during the reaction.

After the long-term testing, the mortar-mixing catalyst exhibited a gradual decrease in reaction rate, which could be ascribed to the slight increase in Au particle size by particles sintering (Supplementary Figs. 42, 43) and the poisoning of Au active site by carbonaceous deposits (Supplementary Figs. 44, 45). Moreover, the significant shift in Au $4f$ binding energy, as shown in Supplementary Fig. 45, is very likely to have originated from the decomposition of tetra-propylammonium hydroxide (TPAOH), which serves as the structure-directing agent for S-1. Furthermore, for the mortar-mixing catalyst ($Au_n:Au_1 = 1:7$), the number ratio of Au SAs to Au NPs can be calculated based on our previous study as 308:1 as seen in the Supplementary Information[44]. Hence, as shown in Fig. 6e, Au NPs can serve as antidote of Au SACs with only trace addition (0.3% ratio of Au SACs) to

simultaneously improve the PO formation rate from 10.4 to 583.6 $mol_{PO}·mol_{Au}^{-1}·h^{-1}$, PO selectivity from 25.1% to 75.6%, and H_2 efficiency from 1.4% – 30.5%, offering a 56-fold, 3-fold, and 22-fold increase, respectively, whose performances can be maintained for 150 h. It is worth noting that these catalysts still encounter certain issues, such as a prolonged induction period and inadequate conversion at low Au loadings. These challenges can potentially be mitigated by selecting calcined S-1 as the catalyst support for achieving precise atomic-level synthesis of Au/S-1 subnanocatalysts with a higher Au loading.

Discussion

In this study, we conduct a proof-of-concept study on the poisoning of Au SACs, and the antidote of Au NPs with only trace addition (0.3% ratio of Au SACs) to reinforce and sustain propylene epoxidation. Although theoretical calculations predict the remarkable epoxidation activity of Au SACs, experimental investigations suggest the
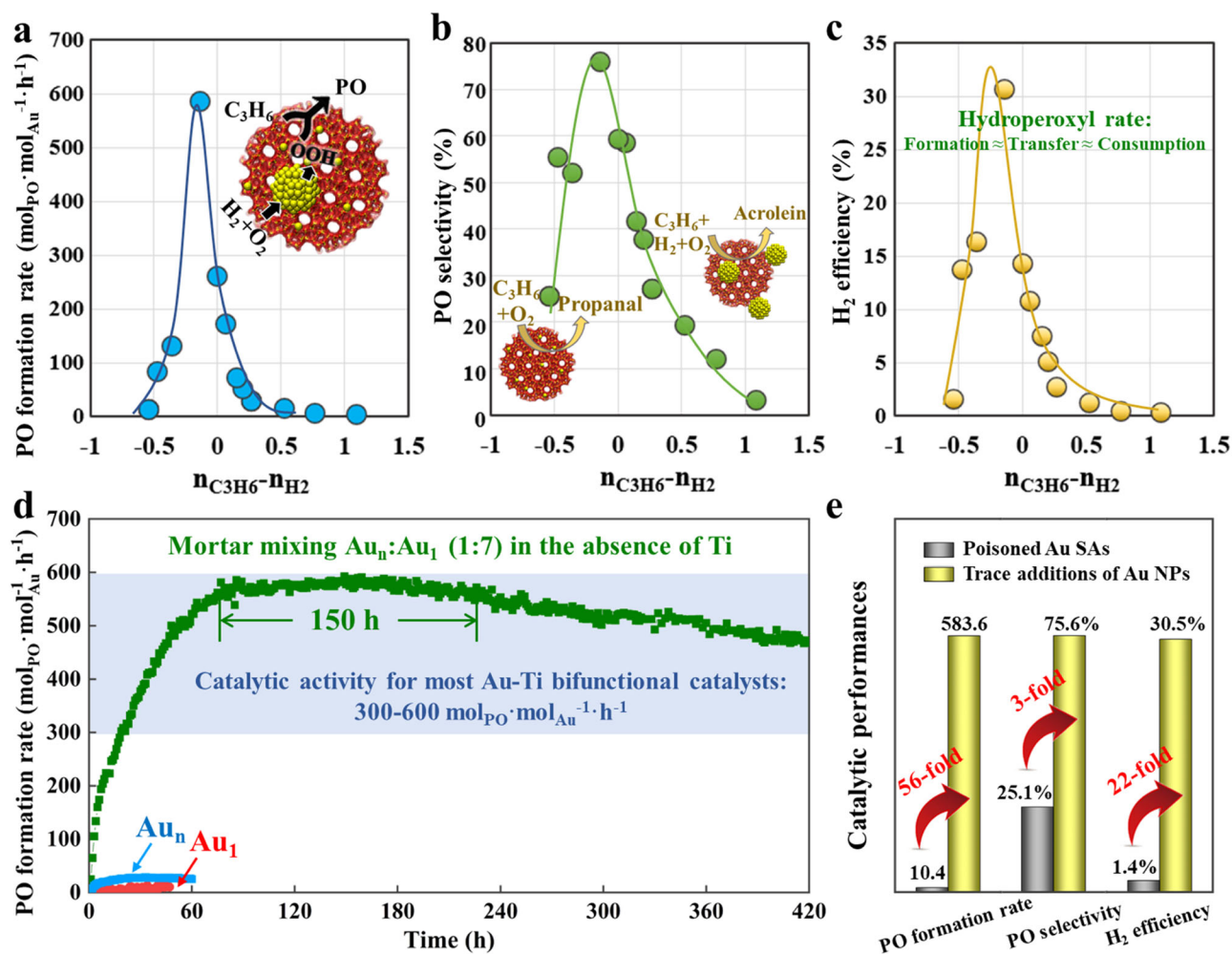
Fig. 6 | Volcano curves and catalytic performances comparison. a–c, PO formation rate (**a**) and selectivity (**b**), as well as H_2 efficiency (**c**) as a function of n_{C3H6}-n_{H2}. **d** Stability test of mortar mixing Au_1 and Au_n in the Au_n/Au_1 mass ratio of 1:7 for propylene epoxidation. **e** Catalytic performances comparison between poisoned Au SAs and those with trace addition of Au NPs (0.3% ratio of Au SACs).

completely opposite kinetics behaviors, including activation energy, reaction orders, and kinetic isotope effects. Further combining multi-scale simulations (DFT and RMD-CMD) formulates a dynamic insight into this contradictory phenomenon, where Au SAs exhibit high catalytic activity at a low C_3H_6 surface coverage, but become poisoned by a solvation layer under a high coverage. In contrast, Au NPs with a weaker binding to C_3H_6 can effectively catalyze H_2 and O_2 to generate the key intermediates of hydroperoxyl radical that can transfer and react with C_3H_6 on Au SAs. Hence, Au NPs can not only help complete the catalytic cycle by reducing C_3H_6 coverage and restoring Au SAs, but also synergistically cooperate with Au SAs by providing different types of active sites required for the activation of H_2/O_2 and C_3H_6. Thus, Au NPs can serve as the antidote for Au SAs to alleviate their poisoning for sustainable PO production, providing the highest catalytic performance of 80.2 $mol_{PO}\cdot mol_{Au}^{-1}\cdot h^{-1}$ of $Au_{1\&n}$ catalyst than the Au_1 (10.4 $mol_{PO}\cdot mol_{Au}^{-1}\cdot h^{-1}$) and Au_n (25.9 $mol_{PO}\cdot mol_{Au}^{-1}\cdot h^{-1}$) catalyst.

A further advancement is made by identifying the difference in reaction order between C_3H_6 to H_2 (n_{C3H6}-n_{H2}) as the catalytic descriptor to establish the volcano curves. It is demonstrated that the reaction is limited by the poisoning adsorption of C_3H_6 at the left side of the volcano curves to produce propanal, while that of H_2 at the right side to yield acrolein. Interestingly, n_{C3H6}-n_{H2} can be fine-tuned by the intimacy and composition of Au SAs and Au NPs to afford the surface coverage-matching between reactants, thus achieving a rate-matching scenario for the formation, transfer, and consumption of hydroperoxyl

radical. As a result, only trace addition of Au NPs (0.3% ratio of Au SACs) enables a simultaneous increase in PO formation rate from 10.4 to 583.6 $mol_{PO}\cdot mol_{Au}^{-1}\cdot h^{-1}$, PO selectivity from 25.1% to 75.6%, and H_2 efficiency from 1.4% to 30.5%, which can be maintained for 150 h. This proof-of-concept study, by introducing trace amounts of antidote to counteract the poisoning of SACs and even reinforce their catalytic performances, demonstrates great potential in accelerating the industrial applications of SACs for a sustainable chemicals production.

Methods
Catalyst preparation
The Ti-free silicalite-1 (S-1) was employed as catalyst support, which was prepared by the hydrothermal method. Typically, 2.00 g poly-oxyethylene 20-sorbitan monolaurate (Tween 20, Sinopharm Chemical Reagent Co., Ltd.) was firstly dissolved in 28 mL ultrapure water, followed by the dropwise addition of 23.00 g TPAOH (25 wt% in water, Shanghai Mindray Chemical Technology Co., Ltd.) under vigorous stirring for 1 h and then 40.53 g tetraethylorthosilicate (TEOS, Shanghai McLean biochemical technology Co., Ltd.) for another 1 h. The as-obtained solution was transferred to a Teflon autoclave, which was heated at 443 K for 48 h under autogenous pressure for crystallization. The crystalline solid was separated from the slurry by centrifugation, subsequently washed and dried at 373 K for 12 h, and the as-obtained sample was directly used as the catalyst support without calcination.

The Au/S-1 catalysts were prepared by the deposition-precipitation-urea method. Typically, 1.00 g S-1 support was mixed with 40.00 mL deionized water under vigorous stirring. Then, a certain amount of 4.85 mM chloroauric acid solution (HAuCl$_4$·4H$_2$O, Sinopharm Chemical Reagent Co., Ltd.) and urea (Shanghai Aladdin Biochemical Technology Co., Ltd.) was added into the above solution, where the molar ratio of chloroauric acid to urea was kept as 1:100. Moreover, the amount of chloroauric acid solution varies from 0.4 mL to 6.0 mL to obtain Au/S-1 catalysts with different sizes. After heating to 363 K under vigorous stirring for another 6 h, the as-obtained catalyst precursor was separated from the slurry by centrifugation, subsequently washed and dried at room temperature overnight under vacuum.

Catalyst characterization

Inductively coupled plasma-atomic emission spectrometry (ICP-AES) analysis was performed on a Varian 710-ES instrument to determined Au loading. X-ray diffraction (XRD) patterns were recorded on a Rigaku D/max2550VB/PC X-ray diffractometer with Cu Kα radiation. High-angle annular dark-field scanning transmission electron microscopy (HAADF-STEM) and element energy-dispersive spectroscopy (EDS) mapping measurements were performed on the ThermoFisher Talos F200X microscope at an operating voltage of 200 kV. Aberration-corrected scanning transmission electron microscopy (AC-STEM) was operated on a ThermoFisher Themis Z transmission electron microscope equipped with two aberration correctors at an operating voltage of 300 kV. To minimize the electron beam damage on zeolite frameworks, a low-damage high angle annular dark field (HAADF)-STEM imaging technique was employed[45]. X-ray photoelectron spectra (XPS) measurements were obtained on an ESCALAB 250 Xi, ThermoFisher with Mg/Al Kα radiation, where all the binding energies were calibrated by the C 1s peak at 284.6 eV. In-situ synchrotron-based FTIR (SR-FTIR) of C$_3$H$_6$ adsorption and desorption experiments were performed on a Nicolet 6700 FTIR Spectrometer with Nicolet Continuum IR Microscope in transmission mode in the Shanghai Synchrotron Radiation Facility (SSRF), Shanghai, China. Firstly, the sample was pretreated under the gas flow (O$_2$:H$_2$:C$_3$H$_6$:N$_2$ = 1:1:1:7) of 30 mL min^{-1} at 200 °C for 1 h. Then, the sample was purged by N$_2$ (30 mL min^{-1}) and cooled down to 40 °C. After the spectra were stable, the background was collected. Afterwards, the gas was switched to the mixture (H$_2$:C$_3$H$_6$:N$_2$ = 1:1:1:7) with the flow rate of 30 mL min^{-1} for 20 min to ensure the saturated adsorption, and further switched back to N$_2$ (30 mL min^{-1}). Finally, the data was collected after the spectra were stable, during which the temperature was increased gradually to 160 °C. The spectra collected at different temperature were subtracted from background spectra at the corresponding temperature. In-situ DRIFTS spectra were collected in an in-situ diffuse reflection cell (Harrick Praying Mantis) placed in PerkinElmer Spectrum 100 FTIR spectrometer, in which the spectra were subtracted from the background spectra.

Catalyst testing

The propylene epoxidation reaction using H$_2$ and O$_2$ was conducted in a fixed bed quartz tubular reactor with an inside diameter of 8 mm under atmospheric pressure. A catalyst weighing 0.15 g and sieved to 200 mesh size was loaded into the reactor and reduced by a H$_2$/N$_2$ mixture (2/3 by volume) with a flow rate of 42 mL·min^{-1} at 583 K for 1.5 h. After cooling the catalyst to 473 K under N$_2$, the reactant mixture containing O$_2$, H$_2$, C$_3$H$_6$, and N$_2$ was introduced with flow rates of 3.5, 3.5, 3.5, and 24.5 mL·min^{-1}, respectively, and a space velocity of 14000 mL·h^{-1}·g$_{cat}$$^{-1}$. The reactant and product components were analyzed using an on-line online mass spectrum (MS) and gas chromatograph (GC) equipped with a TCD detector and FID detector. Oxygenates, such as propylene, PO, acetone, acrolein, and

propanal, were separated using a RT-QS-Bond capillary column (0.35 mm × 30 m) and analyzed with an FID detector. The H$_2$, O$_2$, and CO$_2$ were separated using a TDX-01 column (3 mm × 3 m) and analyzed with a TCD detector.

DFT calculations

All DFT calculations were performed using the Vienna Ab initio Simulation Package (VASP) code[46–48]. The electronic exchange and correlation energy were calculated employing the generalized gradient approximation proposed by Perdew-Burke-Ernzerhof (GGA-PBE)[49]. The projected augmented wave method (PAW) was used to describe the interaction between the ionic cores and valence electrons, with a cut-off energy of 400 eV[50]. The DFT-D3 correction scheme was employed to assess the weak van der Waals interactions between the adsorbed molecules and the catalyst surface[51]. A Monkhorst-Pack grid was used for k-point sampling in the Brillouin zone[52]. Specifically, a 3 × 3 × 1 Monkhorst-Pack k-point mesh within the surface Brillouin zones was used for Au(111) model, while that of 1 × 1 × 1 Monkhorst-Pack k-point mesh for Au single atom and Au$_{13}$ cluster models. A force-based conjugate gradient method was used for geometry optimizations. The transition states of the elementary steps were located by means of the dimer method, and vibrational analyses were further carried out to ensure the local minima and transition states[53]. A threshold of 10^{-5} eV was employed for the convergence of the electronic structure. Convergence of saddle points and minima were believed to reach when the maximum force in each degree of freedom was <0.03 eV · Å^{-1}.

Hybrid classical MD technique and ReaxFF method

A combined reactive force field (ReaxFF) molecular dynamics and classic molecular dynamic simulations were performed using the LAMMPS simulation package[54–56]. Regarding the inert catalyst support of S-1 and the main active species of Au, we used a classical force field to describe the interaction forces between the reactants and Au as well as S-1. To capture the adsorption, diffusion, and reaction behavior, we utilized an Au/C/H/O reaction force field that was optimized based on data obtained from density functional theory (DFT) calculations, which provides a more accurate representation of the Au system and its interactions with carbon, hydrogen, and oxygen. To describe the interactions within the S-1 framework, we employed the Tersoff potential function. This potential function is specifically designed to investigate the structural properties of Si-O systems, making it suitable for modeling the interactions within S-1[57]. Moreover, we have incorporated the two-body Lennard-Jones (LJ) potentials with a cutoff distance of 12 Å to describe the interaction between the S-1 framework and Au catalyst as well as gas molecules. The form of the potential can be written as:

$$\phi_{ij}(r) = \frac{q_i q_j}{r_{ij}} + 4\varepsilon \left[\left(\frac{\sigma}{r_{ij}} \right)^{12} - \left(\frac{\sigma}{r_{ij}} \right)^6 \right] \tag{1}$$

where the corresponding potential parameters can be adopted from the literatures, and summarized in Supplementary Table 8[58,59]. The force field (Au/C/H/O ReaxFF) adapted from the work of Monti et.al. [60]. was applied to properly describe the bond dissociation and formation processes, which can precisely describe the anchoring mechanism of cysteine and gold in an aqueous solution.

Data availability

The authors declare that all the important data to support the findings in this paper are available within the main text or in the Supplementary information. Extra data are available from the corresponding author upon request.

References

1. Qiao, B. et al. Single-atom catalysis of CO oxidation using Pt_1/FeO_x. *Nat. Chem.* **3**, 634–641 (2011).
2. Wang, A., Li, J. & Zhang, T. Heterogeneous single-atom catalysis. *Nat. Rev. Chem.* **2**, 65–81 (2018).
3. Islam, M. J. et al. PdCu single atom alloys supported on alumina for the selective hydrogenation of furfural. *Appl. Catal. B: Environ.* **299**, 120652 (2021).
4. Loy, A. C. M. et al. Elucidation of single atom catalysts for energy and sustainable chemical production: synthesis, characterization and frontier science. *Prog. Energ. Combust.* **96**, 101074 (2023).
5. Ding, S., Hülsey, M. J., Perez-Ramirez, J. & Yan, N. Transforming energy with single-atom catalysts. *Joule* **3**, 2897–2929 (2019).
6. Lu, Y. et al. Identification of the active complex for CO oxidation over single-atom Ir-on-$MgAl_2O_4$ catalysts. *Nat. Catal.* **2**, 149–156 (2019).
7. Niu, H., Zhang, Z., Wang, X., Wan, X., Shao, C. & Guo, Y. Theoretical insights into the mechanism of selective nitrate-to-ammonia electroreduction on single-atom catalysts. *Adv. Funct. Mater.* **31**, 2008533 (2021).
8. Mondelli, C., Gözaydın, G., Yan, N. & Pérez-Ramírez, J. Biomass valorisation over metal-based solid catalysts from nanoparticles to single atoms. *Chem. Soc. Rev.* **49**, 3764–3782 (2020).
9. Lin, J. et al. More active Ir subnanometer clusters than single-atoms for catalytic oxidation of CO at low temperature. *AIChE J.* **63**, 4003–4012 (2017).
10. Ding, K. et al. Identification of active sites in CO oxidation and water-gas shift over supported Pt catalysts. *Science* **350**, 189–192 (2015).
11. Rong, H., Ji, S., Zhang, J., Wang, D. & Li, Y. Synthetic strategies of supported atomic clusters for heterogeneous catalysis. *Nat. Commun.* **11**, 5884 (2020).
12. Zuo, Z. et al. Dry reforming of methane on single-site Ni/MgO catalysts: importance of site confinement. *ACS Catal.* **8**, 9821–9835 (2018).
13. Dong, C. et al. Fully exposed palladium cluster catalysts enable hydrogen production from nitrogen heterocycles. *Nat. Catal.* **5**, 485–493 (2022).
14. Chen, W. et al. Mesokinetics as a tool bridging the microscopic-to-macroscopic transition to rationalize catalyst design. *Acc. Chem. Res.* **55**, 3230–3241 (2022).
15. Liu, Z. et al. Tuning the selectivity of catalytic nitriles hydrogenation by structure regulation in atomically dispersed Pd catalysts. *Nat. Commun.* **12**, 6194 (2021).
16. Zhao, L. et al. A magnetically separable Pd single-atom catalyst for efficient selective hydrogenation of phenylacetylene. *Adv. Mater.* **34**, 2110455 (2022).
17. Arvay, J. W., Hong, W., Li, C., Delgass, W. N., Ribeiro, F. H. & Harris, J. W. Kinetics of propylene epoxidation over extracrystalline gold active sites on Au/TS-1 catalysts. *ACS Catal.* **12**, 10147–10160 (2022).
18. Ishida, T., Murayama, T., Taketoshi, A. & Haruta, M. Importance of size and contact structure of gold nanoparticles for the genesis of unique catalytic processes. *Chem. Rev.* **120**, 464–525 (2020).
19. Lee, W. S., Lai, L. C., Akatay, M. C., Stach, E. A., Ribeiro, F. H. & Delgass, W. N. Probing the gold active sites in Au/TS-1 for gas-phase epoxidation of propylene in the presence of hydrogen and oxygen. *J. Catal.* **296**, 31–42 (2012).
20. Du, W. et al. Kinetic insights into the tandem and simultaneous mechanisms of propylene epoxidation by H_2 and O_2 on Au-Ti catalysts. *ACS Catal.* **13**, 2069–2085 (2023).
21. Lee, W. S., Akatay, M. C., Stach, E. A., Ribeiro, F. H. & Delgass, W. N. Gas-phase epoxidation of propylene in the presence of H_2 and O_2 over small gold ensembles in uncalcined TS-1. *J. Catal.* **313**, 104–112 (2014).
22. Feng, X. et al. Manipulating gold spatial location on titanium silicalite-1 to enhance the catalytic performance for direct propene epoxidation with H_2 and O_2. *ACS Catal.* **8**, 10649–10657 (2018).
23. Zhang, Z. et al. Engineering gold impregnated uncalcined TS-1 to boost catalytic formation of propylene oxide. *Appl. Catal. B: Environ.* **319**, 121837 (2022).
24. Sinha, A. K., Seelan, S., Okumura, M., Akita, T., Tsubota, S. & Haruta, M. Three-dimensional mesoporous titanosilicates prepared by modified sol-gel method: Ideal gold catalyst supports for enhanced propene epoxidation. *J. Phys. Chem. B* **109**, 3956–3965 (2005).
25. Qi, C., Huang, J., Bao, S., Su, H., Akita, T. & Haruta, M. Switching of reactions between hydrogenation and epoxidation of propene over Au/Ti-based oxides in the presence of H_2 and O_2. *J. Catal.* **281**, 12–20 (2011).
26. Huang, J. et al. Propene epoxidation with O_2 and H_2: Identification of the most active gold clusters. *J. Catal.* **278**, 8–15 (2011).
27. Huang, J., Takei, T., Akita, T., Ohashi, H. & Haruta, M. Gold clusters supported on alkaline treated TS-1 for highly efficient propene epoxidation with O_2 and H_2. *Appl. Catal. B: Environ.* **95**, 430–438 (2010).
28. Lu, J., Zhang, X., Bravo-Suárez, J. J., Bando, K. K., Fujitani, T. & Oyama, S. T. Direct propylene epoxidation over barium-promoted Au/Ti-TUD catalysts with H_2 and O_2: Effect of Au particle size. *J. Catal.* **250**, 350–359 (2007).
29. Lee, W. S., Akatay, M. C., Stach, E. A., Ribeiro, F. H. & Delgass, W. N. Enhanced reaction rate for gas-phase epoxidation of propylene using H_2 and O_2 by Cs promotion of Au/TS-1. *J. Catal.* **308**, 98–113 (2013).
30. Barton, D. G. & Podkolzin, S. G. Kinetic study of a direct water synthesis over silica-supported gold nanoparticles. *J. Phys. Chem. B* **109**, 2262–2274 (2005).
31. Joshi, A. M., Delgass, W. N. & Thomson, K. T. Partial oxidation of propylene to propylene oxide over a neutral gold trimer in the gas phase: a density functional theory study. *J. Phys. Chem. B* **110**, 2572–2581 (2006).
32. Zheng, Y. et al. Partial oxidation of propylene with H_2 and O_2 over Au supported on ZrO_2 with different structural and surface properties. *J. Catal.* **401**, 188–199 (2021).
33. Kanungo, S. et al. Silylation enhances the performance of Au/Ti–SiO_2 catalysts in direct epoxidation of propene using H_2 and O_2. *J. Catal.* **344**, 434–444 (2016).
34. Moskaleva, L. V. Theoretical mechanistic insights into propylene epoxidation on Au-based catalysts: Surface O versus OOH as oxidizing agents. *Catal. Today* **278**, 45–55 (2016).
35. Chang, C. R., Wang, Y. G. & Li, J. Theoretical investigations of the catalytic role of water in propene epoxidation on gold nanoclusters: a hydroperoxyl-mediated pathway. *Nano Res* **4**, 131–142 (2011).
36. Peters, S., Peredkov, S., Neeb, M., Eberhardt, W. & Al-Hada, M. Size-dependent XPS spectra of small supported Au-clusters. *Surf. Sci.* **608**, 129–134 (2013).
37. Wang, L. et al. Titanium silicalite-1 zeolite encapsulating Au particles as a catalyst for vapor phase propylene epoxidation with H_2/O_2: a matter of Au–Ti synergic interaction. *J. Mater. Chem. A* **8**, 4428–4436 (2020).
38. Tabor, E., Bernauer, M., Wichterlová, B. & Dedecek, J. Enhancement of propene oligomerization and aromatization by proximate protons in zeolites; FTIR study of the reaction pathway in ZSM-5. *Catal. Sci. Technol.* **9**, 4262–4275 (2019).
39. Tse, E. C. M., Varnell, J. A., Hoang, T. T. H. & Gewirth, A. A. Observation of an inverse kinetic isotope effect in oxygen evolution electrochemistry. *ACS Catal.* **6**, 5706–5714 (2016).
40. Soper, A. K. & Benmore, C. J. Quantum differences between heavy and light water. *Phys. Rev. Lett.* **101**, 065502 (2008).
41. Wang, K. et al. Operando DRIFTS-MS investigation on plasmon-thermal coupling mechanism of CO_2 hydrogenation on Au/TiO_2: the enhanced generation of oxygen vacancies. *Appl. Catal. B: Environ.* **296**, 120341 (2021).

42. Tyagi, A., Matsumoto, T., Kato, T. & Yoshida, H. Direct C–H bond activation of ethers and successive C–C bond formation with benzene by a bifunctional palladium-titania photocatalyst. *Catal. Sci. Technol.* **6**, 4577–4583 (2016).

43. Weisz, P. B. Polyfunctional heterogeneous catalysis. *Adv. Catal.* **13**, 137–190 (1962).

44. Feng, X., Duan, X., Qian, G., Zhou, X., Chen, D. & Yuan, W. Insights into size-dependent activity and active sites of Au nanoparticles supported on TS-1 for propene epoxidation with H_2 and O_2. *J. Catal.* **317**, 99–104 (2014).

45. Tang, X. et al. Atomic insights into the Cu species supported on zeolite for direct oxidation of methane to methanol via low-damage HAADF-STEM. *Adv. Mater.* **35**, 2208504 (2023).

46. Kresse, G. & Furthmüller, J. Efficiency of ab-initio total energy calculations for metals and semiconductors using a plane-wave basis set. *Comput. Mater. Sci.* **6**, 15–50 (1996).

47. Kresse, G. & Furthmüller, J. Efficient iterative schemes for ab initio total-energy calculations using a plane-wave basis set. *Phys. Rev. B* **54**, 11169 (1996).

48. Kresse, G. & Joubert, D. From ultrasoft pseudopotentials to the projector augmented-wave method. *Phys. Rev. B* **59**, 1758 (1999).

49. Perdew, J. P., Burke, K. & Ernzerhof, M. Generalized gradient approximation made simple. *Phys. Rev. Lett.* **77**, 3865–3868 (1996).

50. Blochl, P. E. Projector augmented-wave method. *Phys. Rev. B: Condens. Matter Mater. Phys.* **50**, 17953–17979 (1994).

51. Grimme, S., Antony, J., Ehrlich, S. & Krieg, H. A consistent and accurate ab initio parametrization of density functional dispersion correction (DFT-D) for the 94 elements H-Pu. *J. Chem. Phys.* **132**, 154104 (2010).

52. Methfessel, M. P. A. T. & Paxton, A. T. High-precision sampling for brillouin-zone integration in metals. *Phys. Rev. B* **40**, 3616–3621 (1989).

53. Henkelman, G. & Jónsson, H. A dimer method for finding saddle points on high dimensional potential surfaces using only first derivatives. *J. Chem. Phys.* **111**, 7010–7022 (1999).

54. Thompson, A. P. et al. LAMMPS-a flexible simulation tool for particle-based materials modeling at the atomic, meso, and continuum scales. *Comp. Phys. Comm.* **271**, 108171 (2022).

55. Plimpton, S. Fast parallel algorithms for short-range molecular dynamics. *J. Comput. Phys.* **117**, 1–19 (1995).

56. Aktulga, H. M., Fogarty, J. C., Pandit, S. A. & Grama, A. Y. Parallel reactive molecular dynamics: numerical methods and algorithmic techniques. *Parallel Comput* **38**, 245–259 (2012).

57. Munetoh, S., Motooka, T., Moriguchi, K. & Shintani, A. Interatomic potential for Si-O systems using tersoff parameterization. *Comput. Mater. Sci.* **39**, 334–339 (2007).

58. Calero, S. et al. Understanding the role of sodium during adsorption: a force field for alkanes in sodium-exchanged faujasites. *J. Am. Chem. Soc.* **126**, 11377–11386 (2004).

59. Rappé, A. K., Casewit, C. J., Colwell, K. S., Goddard, W. A. III & Skiff, W. M. UFF, a full periodic table force field for molecular mechanics and molecular dynamics simulations. *J. Am. Chem. Soc.* **114**, 10024–10035 (1992).

60. Monti, S., Carravetta, V. & Ågren, H. Simulation of gold functionalization with cysteine by reactive molecular dynamics. *J. Phys. Chem. Lett.* **7**, 272–276 (2016).

Author contributions

W.C., X.Z. and X.D. conceived this work. W.C., Q.W. and K.S. performed the experiments, collected the data, and wrote the paper. X.Z. and X.D. designed the research, supervised experiments, and edited the paper. C.Liu and C.Lian conducted the density-functional theory calculation and molecular dynamic simulations. T.J. and L.L. helped with in-situ SR-FTIR analyses. Z.Z., G.Q. and J.Z. assisted in the HAADF-STEM and XPS characterization. W.Y. helped with data analyses and discussions. All the authors contributed to the paper revisions.

Competing interests

The authors declare no competing interests.

Additional information

Supplementary information The online version contains supplementary material available at https://doi.org/10.1038/s41467-024-47538-4.

Correspondence and requests for materials should be addressed to Wenyao Chen, Xinggui Zhou or Xuezhi Duan.

Peer review information *Nature Communications* thanks the anonymous reviewers for their contribution to the peer review of this work. A peer review file is available.

Reprints and permissions information is available at http://www.nature.com/reprints

Publisher's note Springer Nature remains neutral with regard to jurisdictional claims in published maps and institutional affiliations.